Electronic Supplementary Material (ESI) for Soft Matter.

Supplementary Information

Magnetocapillary dynamics of amphiphilic Janus particles at curved liquid interfaces

Wenjie Fei[1], Michelle M. Driscoll[2], Paul M. Chaikin[2], and Kyle J. M. Bishop[*1]

[1]Department of Chemical Engineering, Columbia University, New York, NY
[2]Department of Physics, New York University, New York, NY

Contents

[*]Address correspondence to kyle.bishop@columbia.edu

1 Orientation of MJPs at Planar Interfaces

Magnetic Janus particles adsorb at the oil-water interface in a preferred orientation with their MPA-functionalized metal hemisphere in water and their PS hemisphere in oil. We confirmed the particles' orientation using a combination of bright field and fluorescence imaging of MJPs adsorbed at a planar decane-water interface (Fig. S1).

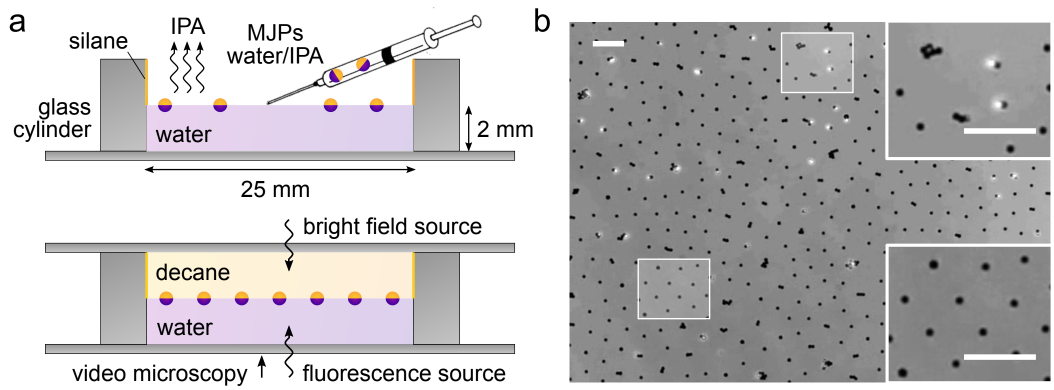

Figure S1: (a) Spreading MJPs on a planar decane-water interface. (b) Combined bright field and fluorescence image of MJPs adsorbed at planar decane-water interface; scale bar is 50 μm

The particles were spread onto the decane-water interface following a literature protocol [1] (Fig. S1a). First, water was added to a cylindrical glass cell mounted on a microscope slide. The top half of the glass cell was treated with a hydrophobic silane to pin the water-decane contact line along a prescribed circular boundary [2]. The volume of water was varied to achieve a nearly planar interface. MJPs were dispersed in a 7:3 mixture of water and isopropyl alcohol (IPA) and injected onto the water-air interface using a Hamilton syringe. Decane was added, and the cell sealed by a glass cover slip using silicon grease.

The particles were imaged from below by an inverted microscope using a combination of bright field and fluorescence imaging modes. Figure S1b shows a characteristic image of MJPs at the decane-water interface. Particles appear dark when their metal hemispheres are oriented "down" toward the aqueous phase and the microscope objective. Alternatively, particles appear bright when oriented "up" such that their fluorescent core is visible. MJPs and small clusters thereof repel one another through electrostatic dipole-dipole interactions to form stable configurations at the interface. Singlet particles are nearly always oriented with their metal hemisphere "down" in agreement with previous reports [1] (Fig. S1b, bottom right). Particle clusters, however, often contain individual particles in other orientations (e.g., the two doublets in Fig. S1b, top right). The application of a uniform magnetic field directed normal to the interface ($B = 15$ mT) had no observable effect on the orientation of the adsorbed MJPs; the magnetic torques were much smaller than those due to interfacial forces.

2 Magnetic Rolling Experiments

To provide an independent estimate of the magnetic moment of the Janus particles, we quantified their translational “rolling” motion above a solid planar substrate due to a rotating magnetic field [3]. As illustrated in Figure S2a, a rotating magnetic field in the xz-plane with magnitude B and frequency ω caused the particle to rotate about the y-axis and simultaneously translate in x-direction. Figure S2b shows the measured particle velocity V as a function of the applied frequency. The velocity increases linearly with frequency up to some critical value ω^*, above which it begins to decrease.

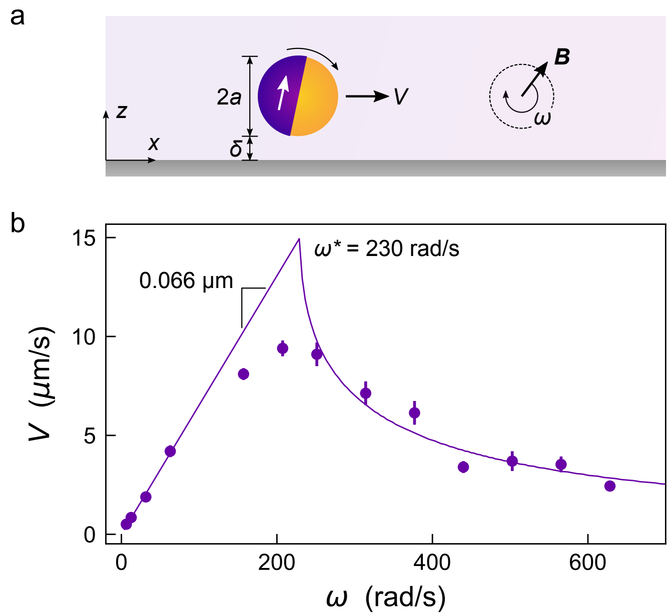

Figure S2: (a) A rotating magnetic field $\boldsymbol{B}(t)$ drives the rotation and translation of a magnetic Janus particle along a solid wall. (b) Measured particle velocity V as a function of the applied frequency ω (markers). The particle radius was $a = 2$ μm, and the field strength $B = 1.7$ mT. Error bars denote the standard error of the measured velocity based on about 100 particles. The solid curve shows the predicted velocity of a ideal ferromagnetic sphere with magnetic moment $m = 3.1 \times 10^{-14}$ A m^2.

This observed behavior is captured quantitatively by a model that accounts for the magnetic and viscous torques acting on the particle and for the hydrodynamic coupling between particle rotation and translation near the solid substrate [3]. Below the critical frequency, the particle's magnetic moment rotates in lock step with the applied field such that the angular velocity of the particle is equal to that of the field. At low Reynolds numbers, the resulting particle velocity is given by

$$V = a\omega \frac{Y^B(\xi)}{Y^A(\xi)} \quad \text{for } \omega < \omega^*, \tag{S1}$$

where Y^A and Y^B are components of the hydrodynamic resistance tensor for a sphere separated from a plane wall by a scaled distance $\xi = \delta/a$ [4, 5]. From the experimental data, the fitted slope of the particle velocity versus applied frequency is 0.066 μm for $a = 2$ μm. Using these values, eq. (S1) implies that the effective surface separation is $\xi = 0.21$. At the critical frequency, the viscous torque on the particle is equal to the maximum magnetic torque such that

$$6\pi\eta a^3 \omega^* Y^C(\xi) = mB, \tag{S2}$$

where the coefficient Y^C describes the torque on a sphere rotating about an axis parallel to the surface [6] (here, $Y^C = 1.69$ for the estimated surface separation $\xi = 0.21$). Using the known viscosity ($\eta = 8.90 \times 10^{-4}$ Pa s) and field strength ($B = 1.7$ mT), eq. (S2) implies that the particle magnetic moment is $m = 3.1 \times 10^{-14}$ A m^2.

3 Characterization the Uniform Magnetic Field

We designed and built a two-coil electromagnet for manipulating MJPs on the stage of an inverted optical microscope. Each coil was prepared by winding 131 m of copper wire with an insulating coating (24 AWG) around a 3D-printed ABS scaffold with an inner diameter of 3.4 cm, outer diameter of 9.4 cm, and height of 1.2 cm. The wrapped wire had an inner diameter of 3.6 cm, outer diameter of 9.3 cm, and height of 0.8 cm. The two coils were 1.8 cm apart from each other and placed above and below an acrylic sample holder mounted on the microscope stage (Fig. S3a). The water drops on which the particles moved were positioned at the center of the two coils. DC currents of 0.25 to 0.9 A were applied to the coils using a sourcemeter unit (Keithely 2410). The resulting magnetic field was measured at different locations using a gaussmeter (AlphaLab Inc. Model GM2). Figures S3b and S3c show the two components, B_z and B_r, of the axially symmetric magnetic field for an applied current of 0.9 A. Within the 0.4 cm^3 region of interest (Fig. S3a, red region), variations in the applied field were ca. 0.5% of the maximum field strength.

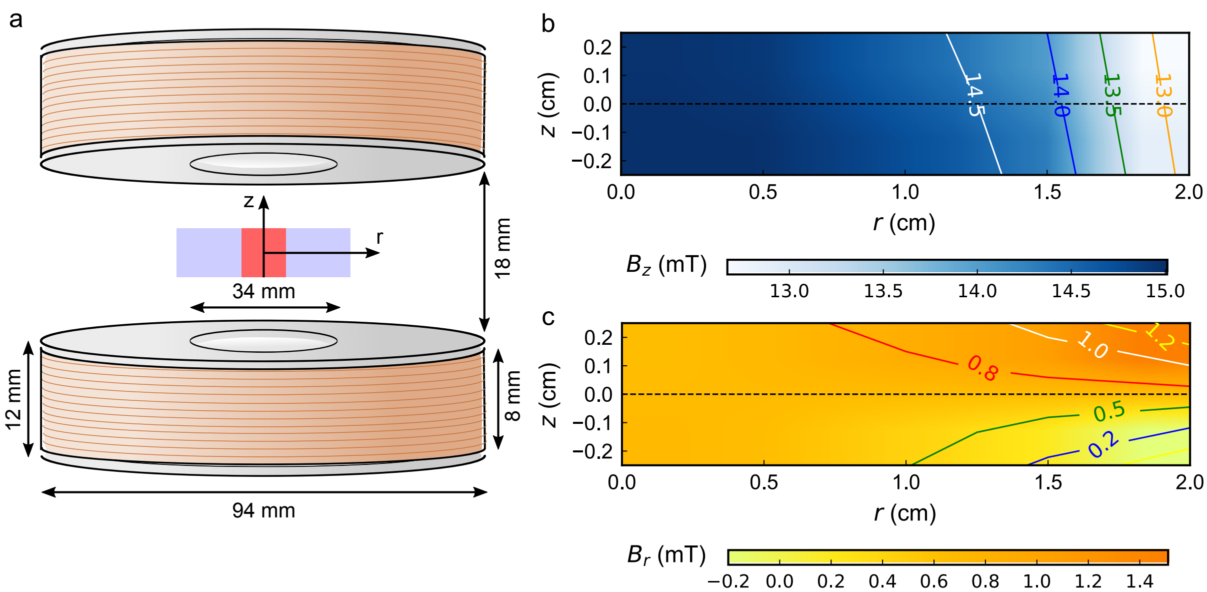

Figure S3: (a) Schematic illustration of the electromagnet design. The center of the drop was located at $r = 0$ cm and $x = 0$ cm during each experiment. The measurement region is colored in blue and the region of interest in red. (b,c) Measured components of the magnetic field (b) B_z and (c) B_r as a function of position between the two coils. The component B_r was measured along one direction perpendicular to the z-axis.

4 Model of Particle Dynamics with Gravity

As in the main text, we consider an amphiphilic Janus sphere of radius a with permanent magnetic moment $\boldsymbol{m}$ adsorbed at the interface of a spherical drop of radius R (Fig. 2). We now consider the effects of a gravitational field pointing in the positive z-direction, parallel to the applied magnetic field $\boldsymbol{B}$.[1] Using a spherical coordinate system centered on drop, the total energy of the particle in these two fields is approximated as

$$U = mB\left(\cos\beta\sin\alpha\sin\theta - \cos\alpha\cos\theta\right) - MgR\cos\theta, \tag{S3}$$

where m and M are, respectively, the magnetic moment and buoyant mass of the particle, and g is the acceleration due to gravity. From this expression, we derive the generalized forces that act to move and rotate the Janus particle on the drop interface. In the overdamped regime, the resulting particle dynamics are expressed as

$$\dot{\theta} = -\frac{1}{\lambda_t R^2}\frac{\partial U}{\partial \theta} = -\frac{mB}{\lambda_t R^2}\left(\sin\alpha\cos\beta\cos\theta + \cos\alpha\sin\theta\right) - \frac{Mg}{\lambda_t R}\sin\theta, \tag{S4}$$

$$\dot{\beta} = -\frac{1}{\lambda_r}\frac{\partial U}{\partial \beta} = \frac{mB}{\lambda_r}\sin\alpha\sin\beta\sin\theta, \tag{S5}$$

For small particles ($a \ll R$) with magnetic moments oriented parallel to the interface ($\alpha = \pi/2$), the orientation angle β relaxes quickly to a stable value of $\beta = \pi$. The dynamics of the particle position, characterized by the polar angle θ, can be approximated as

$$\dot{\theta} = k_m\cos\theta - k_g\sin\theta, \tag{S6}$$

where $k_m \equiv mB/\lambda_t R^2$ and $k_g \equiv Mg/\lambda_t R$ are characteristic rates due to magnetic and gravitational forces, respectively. These dynamics are characterized by a stable particle position θ_s at which gravitational and magnetic forces are balanced, $\theta_s = \cot^{-1}(k_g/k_m)$. The system approaches this final position with a characteristic rate constant $k = (k_m^2 + k_g^2)^{1/2}$. When the particle starts from the position of lowest gravitational energy ($\theta(0) = 0$), the approximate dynamics of eq. (S6) can be integrated to obtain

$$\theta(t) = -2\tan^{-1}\left\{G - \sqrt{G^2+1}\tanh\left[\frac{1}{2}kt + \tanh^{-1}\left(\frac{G}{\sqrt{G^2+1}}\right)\right]\right\}, \tag{S7}$$

where $G \equiv k_g/k_m = MgR/mB$ is a dimensionless parameter characterizing the relative importance of gravitational and magnetic forces. The projected radial position measured experimentally is $r(t) = R\sin\theta(t)$. Figure S4 shows the computed dynamics for different gravitational strengths G.

[1] It is only for mathematical convenience that the gravitational field is directed in the positive z-direction and not the negative z-direction as in experiment. This choice confines the relevant particle motions to the region $0 < \theta < \pi/2$ (as opposed to $\pi/2 < \theta < \pi$).

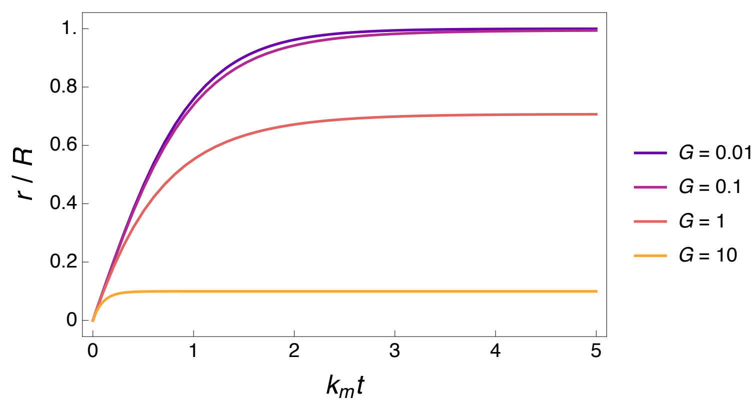

Figure S4: Projected radial position as a function of time for different gravitational strengths, $G = MgR/mB$. Initially, the particle is positioned at gravitational energy minimimum $\theta(0) = 0$. Here, the radial position is scaled by the drop radius R; time is scaled using the magnetic rate constant $k_m = mB/\lambda_t R^2$.

5 Data Analysis

5.1 Parsing Raw Track Data

As discussed in the main text, other forces acting on the MJPs can become significant when the magneto-capillary forces are sufficiently weak. Even at the highest field strengths of $B = 15$ mT, magnetic forces become progressively weaker as the particle approaches its equilibrium position at the drop equator. As a result, particles were often observed to deviate from their expected radial trajectories near the drop equator (Fig. S5). Such behaviors are not described by our magneto-capillary model and can interfere with our estimate of the rate parameter k_m. The track data were therefore cropped to exclude these anomalous portions of the particle trajectory.

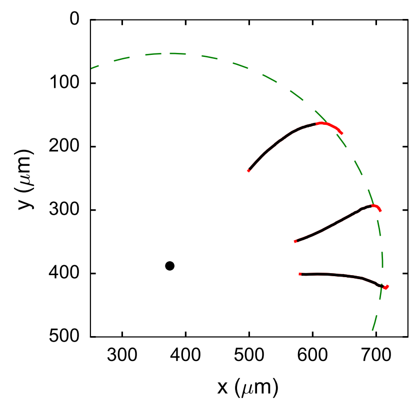

Figure S5: Three trajectories of a single MJP projected onto the xy-plane (red). The dashed circle shows the perimeter of the drop centered on the black dot with radius $R = 335$ μm. Only the black portions of the trajectories are used to fit the model parameter.

5.2 Parameter Estimation of k_m

To estimate the magnetic rate parameter k_m, we use the following model for the projected particle position as a function of time,

$$\begin{aligned} x(t) &= x_o + r(t)\cos\varphi + \varepsilon, \\ y(t) &= y_o + r(t)\sin\varphi + \varepsilon. \end{aligned} \tag{S8}$$

Here, (x_o, y_o) and φ are, respectively, the origin and the angle the radial trajectory, and ε is a normally distributed random variable with zero mean and standard deviation Δ. The radial position of the particle is given by

$$r(t) = R\sin\left\{2\tan^{-1}\left[\tanh\left(\frac{1}{2}k_m t + C\right)\right]\right\}, \tag{S9}$$

where R is the drop radius, and $C > 0$ is a positive constant that specifies the radial position at time $t = 0$.

During each experiment, we measure the particle position (x_k, y_k) at successive times t_k following the application of the magnetic field. From these data $\boldsymbol{D}$, we use Bayes theorem to estimate the probability distribution for the unknown parameters $\boldsymbol{X}$ as

$$\text{prob}(\boldsymbol{X} \mid \boldsymbol{D}) \propto \text{prob}(\boldsymbol{D} \mid \boldsymbol{X})\,\text{prob}(\boldsymbol{X}). \tag{S10}$$

The posterior distribution, prob$(\boldsymbol{X} \mid \boldsymbol{D})$, is sampled using Markov Chain Monte Carlo (MCMC) in pyMC3 [7]. The likelihood function, prob$(\boldsymbol{D} \mid \boldsymbol{X})$, assumes that the observed quantities (x_k, y_k) are independent, normally distributed random variables with unknown standard deviation Δ due to measurement error. The prior probability distribution, prob($\boldsymbol{X}$), captures our knowledge of the unknown parameters before analyzing the tracking data.

Specifically, the prior for the rate constant k_m is chosen as a log-normal distribution with parameters $\mu = \ln k'_m$ and $\sigma = 0.5$, where k'_m denotes the theoretical prediction. This choice implies that the rate parameter is positive and within an order-of-magnitude of the model prediction. The prior for C is also log-normal with $\mu = \ln C'$ and $\sigma = 0.5$, where $C' = 0.27$ such that $r(0) = 0.5R$. The prior for the noise Δ is log-normal with $\mu = \ln \Delta'$ and $\sigma = 0.5$, where $\Delta' = 1$ μm. The drop radius R is measured from an image focused on the drop equator using the Hough circle transformation in ImageJ. This procedure also provides an estimate for the drop center (x'_o, y'_o), which differs somewhat from the origin of the radial particle trajectories. The priors for x_o and y_o are normal distributions with standard deviation $\sigma = 30$ μm about the measured drop center (x'_o, y'_o). The prior for the angle φ is also normal with standard deviation $\sigma = \pi/4$.

For each drop, particle, and field strength, we obtained several particle trajectories (typically, 3 to 9). The rate parameter k_m, drop center (x_o, y_o), and noise Δ were assumed to be common to all of these trajectories; however, the constant C and the angle ϕ were allowed to vary one trajectory to the next (see Fig. S5). The parameters were sampled from the distribution (S10) using 2000 iterations of the No-U-Turn Sampler (NUTS) implemented in pyMC3. The mean values of the sampled parameters were used to collapse the data shown in Figures 3a and 3c; the markers in Figures 3b and 3d represent mean values of the sampled rate parameter.

5.3 Sedimentation

To assess the effects of gravity on the motion of MJPs, we first consider the sedimentation of the particles along the drop interface in the absence of the magnetic field. Following the approach of section 4, the position of a particle on the drop surface will evolve under gravity as

$$\dot{\theta} = -k_g \sin\theta, \tag{S11}$$

where $k_g = Mg/\lambda_t R$ is the gravitational rate parameter. Note that this expression assumes that the gravitational energy minimum occurs at $\theta = 0$ (not $\theta = \pi$ as in our experiments); this difference does not affect the projected radial position $r = R\sin(\theta)$. Integrating eq (S11), we obtain the predicted radial trajectory

$$r(t) = R\,\mathrm{sech}(k_g t + C), \tag{S12}$$

where $C > 0$ is a positive constant that determines the particle position at time $t = 0$.

Using this model, we analyzed the multiple trajectories of four different particles sedimenting along the interface of four drops of different sizes (Fig. S6a-d). The model agrees with the data at early times, but deviates significantly at later times as the particle begins to interact with the underlying substrate, the three-phase contact line, and any other particles pinned there. Therefore, we focus our analysis exclusively on the data in this early time period. Figure S7 shows that the inferred rate parameter k_g decreases with increasing drop size. Accounting for variability in the rate parameter from particle-to-particle (see discussion below), the data agree with the model predictions. The buoyant mass inferred from the fit in Figure S7 is $M = 6.3 \times 10^{-15}$ kg, which is roughly two times smaller than the calculated buoyant mass 1.4×10^{-14} kg.

5.4 Magnetic actuation with gravity

To assess the role of gravity in explaining our experimental observations, we analyzed the data from Figure 3 using the augmented model described Section 4. In this analysis, the gravitational rate parameter k_g was taken directly from our analysis of the sedimentation in Section 5.3. We used the same Bayesian MCMC approach detailed in Section 5.2. Figure S8 shows the inferred rate parameter k_m accounting for effects due to gravity force. Even at the weakest fields, the forces due to gravity are still much smaller than those due to the magnetic field ($G = 0.2 \ll 1$). Consequently, there is only a small change in the inferred rate parameter as compared to that derived using the simpler model that neglects gravitational effects.

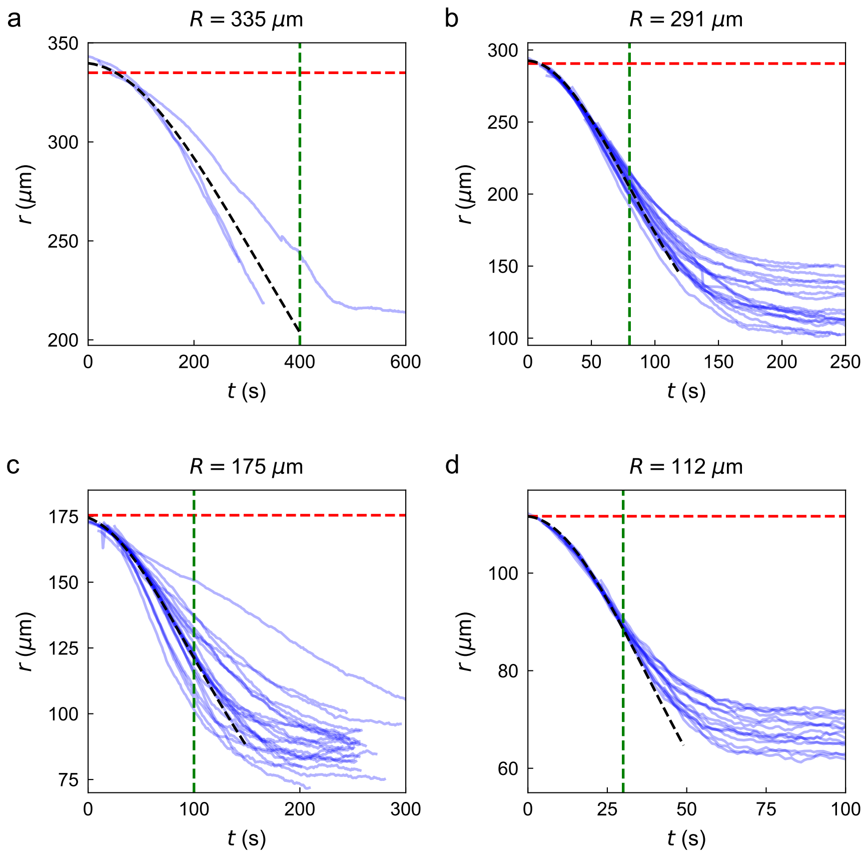

Figure S6: Projected radial position as a function of time for four particles sedimenting along the interface of four droplets of different sizes. The model fit (black curve) is based only on data at early times (green line); the red line denotes the drop radius.

5.5 Variability in Rate Parameter

The variability in particle motions from one particle to the next was assessed using three independent data sets. First and perhaps most directly, we examined the dynamics of multiple particles migrating simultaneously on the same drop when subject to the applied field (Supporting Video 1).[2] For each of the six particles, we estimated the rate parameter k_m from the reconstructed particle trajectory as described in Section 5.2. To facilitate the comparison of rate parameters for different conditions spanning orders of magnitude, we will assume that variations in the rate parameter are log-normally distributed with parameters μ_0 and σ_0. Taking the standard deviation of the logarithm of estimates for k_m, we estimate that $\sigma_0 = 0.55$.

Additionally, we analyzed the data in Figure 3b and Figure S8 to provide additional estimates of the particle-to-particle variability. Specifically, we modelled the rate parameters k_m in Figure 3b as log-normally distributed with parameters $\mu_1 = C_1/R^2$ and σ_1, where R is the drop radius, and C_1 and σ are unknown constants to be determined by the fitting procedure. Similarly, we modelled the gravitational rate parameters k_g in Figure S8 as log-normally distributed with parameters $\mu_2 = C_2/R$ and σ_2. Using Bayesian inference with MCMC sampling, we derived the following estimates for the parameters $\sigma_1 = 0.47$ and $\sigma_2 = 0.63$. These estimates are very similar to that obtained from multiple particles under identical conditions. Ultimately, we conclude that the dynamics of different particles can vary by a factor of $e^{\sigma} = 1.7$. Interestingly, this conclusion applies to particle dynamics driven by magnetic fields and by gravity alone, which suggests that the variations in the drag coefficient λ_t might be responsible (e.g., due to fluctuations in the three-phase contact line [8].

[2] This video was captured in bright-field mode in contrast to the other videos we analyzed, which were captured using fluorescence imaging.

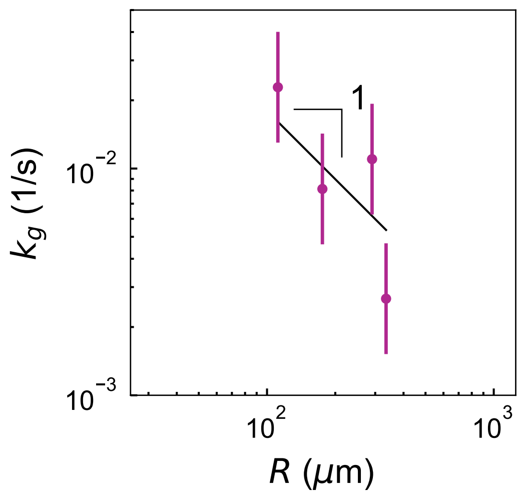

Figure S7: Gravitational rate parameter k_g as a function of drop radius as infer from the data in Fig. S6. Error bars denote the standard deviationf of the measured rate constant k_g based on 3 to 19 particle trajectories.

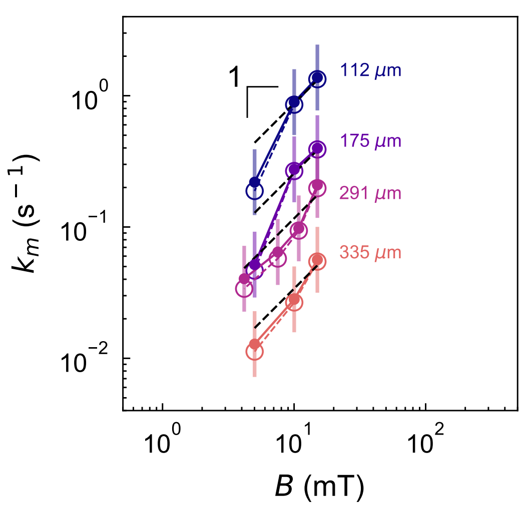

Figure S8: Magnetic rate parameter k_m inferred using a model that accounts for magnetic and gravitational forces on the particle. Open markers shows the rate constants k_m from Figure 3, where gravity was not considered.

References

1. Park, B. J., Brugarolas, T. & Lee, D. Janus particles at an oil–water interface. *Soft Matter* **7,** 6413–6413 (2011).
2. Reynaert, S., Moldenaers, P. & Vermant, J. Control over Colloidal Aggregation in Monolayers of Latex Particles at the Oil–Water Interface. *Langmuir* **22,** 4936–4945 (2006).
3. Driscoll, M., Delmotte, B., Youssef, M., Sacanna, S., Donev, A. & Chaikin, P. Unstable fronts and stable "critters" formed by microrollers. *Nat. Phys.* **13,** 375–380 (2017).
4. O'neill, M. E. A slow motion of viscous liquid caused by a slowly moving solid sphere. *Mathematika* **11,** 67–74 (1964).
5. Goldman, A. A., Cox, R. G. R., Brenner, H. & Goldmans, A. J. Slow viscous motion of a sphere parallel to a plane wall—I Motion through a quiescent fluid. *Chem. Eng. Sci.* **22,** 637–651 (1967).
6. Dean, W. W. & O'Neill, M. M. A slow motion of viscous liquid caused by the rotation of a solid sphere. *Mathematika* **10,** 13–24 (1963).
7. Salvatier, J., Wiecki, T. & Fonnesbeck, C. Probabilistic Programming in Python using PyMC. *PeerJ Comput. Sci.* **2,** e55 (2016).
8. Boniello, G., Blanc, C., Fedorenko, D., Medfai, M., Mbarek, N. B., In, M., Gross, M., Stocco, A. & Nobili, M. Brownian diffusion of a partially wetted colloid. *Nat. Mater.* **14,** 908–911 (2015).